

Iterated Invariant EKF for 3D Landmark-Aided Inertial Navigation ^{*}

Hilton Marques Souza Santana¹[0000-0002-2840-2904], João Carlos Virgolino Soares²[0000-0002-6278-378X], and Marco Antonio Meggiolaro¹[0000-0002-6240-8189]

¹ Pontifical Catholic University of Rio de Janeiro, Rio de Janeiro, Brazil
hiltonmarques@gmail.com

² Dynamic Legged Systems Lab, Istituto Italiano di Tecnologia, Genova, Italy

Abstract. Inertial navigation systems aided by three-dimensional landmark measurements constitute a fundamental problem in robotic perception and state estimation. Classical $SO(3)$ -based Extended Kalman Filter ($SO(3)$ -EKF) approaches provide practical solutions, but suffer from the false observability problem, in which the filter becomes overconfident in unobservable directions, leading to degraded estimation performance. The Invariant EKF (IEKF) addresses this limitation by reformulating the system dynamics as a group-affine system on a Lie group, although its measurement update does not fully satisfy certain state compatibility properties. More recently, the Iterated Invariant EKF (IterIEKF) was proposed to further improve the IEKF by ensuring, in the low-noise regime, that the estimated state remains on the observed state manifold while the uncertainty is confined to its tangent space. In this work, we formulate and apply the IterIEKF to landmark-based inertial 3D localization for the first time. Through numerical simulations, we show that the proposed approach outperforms the classical $SO(3)$ -EKF, the Iterated $SO(3)$ -EKF, and the IEKF in terms of both estimation accuracy and consistency.

Keywords: Kalman Filter · Localization · Sensor Fusion.

1 Introduction

The necessity of estimating the state of a mobile system, including its position, orientation, and velocity, has been a fundamental challenge throughout the history of navigation. The use of celestial landmarks for localization spans several millennia. In particular, mariners in the Northern Hemisphere estimated their latitude by measuring the elevation of the North Star (Polaris) above the horizon [1, pg. 2]. These early navigation techniques relied on identifiable, static features in the environment, giving rise to the modern notion of landmarks as fixed

^{*} This study was financed in part by the Coordenação de Aperfeiçoamento de Pessoal de Nível Superior – Brasil (CAPES) – Finance Code 001 and the Fundação de Amparo à Pesquisa do Estado do Rio de Janeiro (FAPERJ).

reference points that can be repeatedly observed to infer an agent’s state. During the mid-twentieth century, the success of the Apollo missions demonstrated that robust navigation required not only observations of external landmarks, such as stars, but also accurate inertial measurements from accelerometers and gyroscopes. The fusion of inertial and exteroceptive sensing established many of the principles that underpin modern state estimation. Since the early 2000s, the emergence of Micro Aerial Vehicles (MAVs), together with the widespread availability of sophisticated sensing technologies, including RGB-D cameras, LiDARs, and high-performance embedded computing platforms, has enabled real-time state estimation and map reconstruction in increasingly complex environments [11]. These technological advances have made it practical to address the Simultaneous Localization and Mapping problem [9].

The classical algorithmic foundation for landmark-based localization for autonomous mobile robots was established in [14]. This framework relies on two key stages: landmark detection within the scene, followed by data association (or matching), which evaluates whether an observed feature has been previously cataloged or represents a new landmark. In this work, we consider a 3D MAV navigating with inertial sensors through an environment where a prior map has already been constructed and features are uniquely identifiable, meaning the underlying data association problem is assumed to be solved. Then, we combine exteroceptive updates (measurements of known landmarks) and proprioceptive inputs (inertial measurements), also called Visual-Inertial Odometry (VIO), through a unified probabilistic framework in order to obtain a real-time state estimate of the robot.

Probabilistic filtering methods, particularly those based on the Extended Kalman Filter (EKF), have played a central role in landmark-aided inertial navigation over the past decades. One of its earliest applications to inertial navigation with a vehicle equipped with an Inertial Measurement Unit (IMU) and capable of autonomously measuring its relative position with respect to a pre-built three-dimensional map was presented in [21]. That work formulated an $SO(3)$ -EKF (also known as Multiplicative-EKF or Quaternion-EKF [16]) for the precision landing of a spacecraft using observations of known planetary landmarks. Subsequently, Li and Mourikis [15] showed that this standard formulation suffers from the so-called false observability problem, motivating the development of constrained filters. Later, a seminal study by Barrau and Bonnabel [2] demonstrated that false observability fundamentally arises from the choice of error-state parameterization and can be mitigated by exploiting the symmetry of the underlying system through the Invariant Extended Kalman Filter (IEKF). The IEKF was later applied to indoor MAV navigation in [6], where it demonstrated superior estimation performance compared to conventional EKF formulations. Nevertheless, the classical IEKF still relies on a first-order linearization of the measurement model about the predicted state, which may degrade estimation accuracy in highly nonlinear scenarios. To overcome this limitation, Goffin et al. [12] proposed the Iterated IEKF (IterIEKF), which performs a sequence of local optimization steps to estimate the mode of the posterior distribution while

reducing the impact of first-order approximation errors. The IterIEKF has recently demonstrated improved convergence properties for state estimation of a quadrupedal robot in [17].

In this work, we apply the IterIEKF framework for the first time to a MAV equipped with an IMU capable of measuring its relative position to known environmental landmarks. Through extensive Monte Carlo simulations evaluated on one of the EuRoC MAV datasets [7], we demonstrate that the IterIEKF outperforms the standard SO(3)-EKF, its iterated variant (IterSO(3)-EKF), and the standard IEKF in terms of state estimation accuracy and statistical consistency. More specifically, the primary contributions of this paper are summarized as follows:

- We derive complete mathematical formulations of both invariant and multiplicative iterated filters tailored for landmark-aided MAV state estimation. To the best of our knowledge, the complete algorithmic derivation of the IterIEKF in this specific framework is presented here for the first time.
- We provide a systematic comparative study analyzing the direct impact of iterative invariant updates on both the trajectory accuracy and the statistical consistency of the estimated states. Through controlled Monte Carlo trials, we demonstrate that the IterIEKF yields substantial improvements in consistency metrics, resulting in an error reduction of approximately 80% in the estimated position and linear velocity vectors.
- We present an in-depth analysis of online IMU bias estimation dynamics, demonstrating that while the accelerometer bias remains difficult to fully observe across all evaluated filters, the IterIEKF consistently achieves the most accurate profile overall.

The work will be structured as follows. In Section 2, we provide a comprehensive review of the relevant literature, highlighting the key contributions and limitations of existing approaches. Section 3 introduces the mathematical background necessary for understanding the described filters. Section 4 details a simple example that highlights the geometrical aspect behind IterIEKF. From Sections 5 to 8 we describe all filter derivations, including the SO(3)-EKF, IterSO(3)-EKF, IEKF, and IterIEKF. In Section 9 we present the results of our Monte Carlo experiments, comparing the performance of the different filters in terms of accuracy and consistency. Finally, we conclude with a discussion of our findings and potential directions for future research in Section 10.

2 Related Work

The landscape of visual-inertial state estimation has evolved significantly, shifting from traditional local coordinate representations to geometrically principled invariant frameworks and high-fidelity iterative updates.

2.1 Multiplicative and Invariant Visual-Inertial Estimators

Early frameworks for landmark-aided localization primarily focused on absolute positioning and landing applications. For instance, Trawny et al. [21] developed a

vision-aided inertial navigation system specifically optimized for pin-point landing, relying on observations of pre-mapped landmarks. While highly effective for localized target tracking, classical $SO(3)$ -EKF frameworks are fundamentally hindered by consistency issues. This limitation was thoroughly dissected by Li and Mourikis [15], who demonstrated that conventional VIO formulations suffer from false observability, where the filter erroneously gains information along unobservable directions, such as yaw and global position, leading to overoptimistic covariance estimates and degraded accuracy.

To resolve these consistency mismatches, Barrau and Bonnabel introduced the IEKF framework [2]. Later, Brossard et al. [6] applied it directly to visual-inertial SLAM. By parameterizing the state error using Lie group actions, the IEKF guarantees that the error kinematics remain independent of the robot’s absolute trajectory. This mathematical property inherently eliminates the false observability problem without requiring artificial modifications like First-Estimates Jacobians. Our work builds directly upon this invariant paradigm, extending it from a single-step propagation-update loop to an optimization-driven iterative routine tailored for MAV setups.

2.2 Iterated and Manifold-Based Filtering

Parallel to the development of invariant filtering, iterated Kalman filters emerged as an effective approach to reduce the linearization errors introduced by highly nonlinear measurement models. In the context of visual-inertial odometry, Bloesch et al. [4] proposed an iterated EKF that combines direct photometric feedback with manifold-based state representations for rotations and landmark bearing vectors, improving robustness through iterative measurement refinement. Later, He et al. [13] generalized this methodology into a canonical framework for Kalman filtering on differentiable manifolds, enabling generic iterated error-state filters on arbitrary product manifolds. However, neither approach explicitly addresses the consistency issues arising from the incorrect linearization of unobservable directions, and therefore, they do not resolve the false-observability problem.

Bridging the gap between geometric tracking and invariant filtering, Goffin et al. [12] introduced the Iterated IEKF. By fusing Lie group invariance with manifold-aware Gauss-Newton iterations, the IterIEKF solves the maximum a posteriori (MAP) estimation problem while confining uncertainty in the tangent space of the observed submanifold. While their initial framework demonstrated remarkable performance on legged quadrupedal platforms [17], its application to unconstrained, high-velocity 3D aerial robotics has yet to be fully explored.

In contrast to the aforementioned literature, this paper presents the first explicit application and evaluation of the IterIEKF for a 3D MAV executing navigation loops via relative position observations to mapped landmarks. Unlike traditional VIO methods [21, 15] that suffer from false observability, and conventional iterated manifold filters [4, 13] that lack invariant error dynamics, our formulation combines the statistical consistency of invariant mechanics with the high-accuracy tracking of iterated update steps. We provide a rigorous,

simulation-backed verification of this approach under extensive Monte Carlo trials, explicitly detailing the filter’s superiority in state accuracy, consistency, and online IMU bias estimation.

3 Mathematical Background

We define the robot true state at instant t_i as being the orientation ($\mathbf{R}_i \in \text{SO}(3)$), base velocity ($\mathbf{v}_i \in \mathbb{R}^3$), position ($\mathbf{p}_i \in \mathbb{R}^3$), all relative to the world frame, and IMU gyroscope and accelerometer bias ($\mathbf{b}_g, \mathbf{b}_a \in \mathbb{R}^3$). In this work, the robot state is embedded into two distinct matrix Lie groups, $\text{SE}_2(3) \times \mathbb{R}^6$ [6] and $\text{SO}(3) \times \mathbb{R}^{12}$ [21]:

$$\mathcal{X}_i := \begin{bmatrix} \begin{bmatrix} \mathbf{R}_i & \mathbf{v}_i & \mathbf{p}_i \\ \mathbf{0}_{1,3} & 1 & 0 \\ \mathbf{0}_{1,3} & 0 & 1 \end{bmatrix} & \mathbf{0}_{5,7} \\ \mathbf{0}_{7,5} & \begin{bmatrix} \mathbf{I}_6 & \begin{bmatrix} \mathbf{b}_{g,i} \\ \mathbf{b}_{a,i} \end{bmatrix} \\ \mathbf{0}_{1,6} & 1 \end{bmatrix} \end{bmatrix} \in \text{SE}_2(3) \times \mathbb{R}^6, \quad (1)$$

$$\mathbf{x}_i := \{\mathbf{R}_i, \mathbf{v}_i, \mathbf{p}_i, \mathbf{b}_{g,i}, \mathbf{b}_{a,i}\} \in \text{SO}(3) \times \mathbb{R}^{12}.$$

Every matrix Lie group G has an associated Lie algebra \mathfrak{g} of the same dimension n . We define the isomorphisms between \mathfrak{g} and \mathbb{R}^n as:

$$\text{Hat} : \mathbb{R}^n \rightarrow \mathfrak{g}, \quad \mathbf{v} \mapsto \mathbf{v}^\wedge = \sum_{i=1}^n v_i E_i, \quad (2)$$

$$\text{Vee} : \mathfrak{g} \rightarrow \mathbb{R}^n, \quad \mathbf{v}^\wedge \mapsto (\mathbf{v}^\wedge)^\vee = \mathbf{v} = \sum_{i=1}^n v_i \mathbf{e}_i, \quad (3)$$

where $\{E_i\}$ and $\{\mathbf{e}_i\}$ are bases for \mathfrak{g} and \mathbb{R}^n . In this work, we use the \mathbb{R}^n representation of \mathfrak{g} . Both spaces are related by the local homeomorphism $\exp_G : \mathfrak{g} \rightarrow G$, where $\mathbf{v}^\wedge \mapsto \exp_G(\mathbf{v}^\wedge) = \sum_{i=0}^{\infty} \frac{\mathbf{v}^{\wedge i}}{i!}$, and its inverse $\log_G : G \rightarrow \mathfrak{g}$. We define $\text{Exp}_G(\mathbf{v}) := \exp_G(\mathbf{v}^\wedge)$ and $\text{Log}_G(\mathcal{X}) := \log_G(\mathcal{X})^\vee$ for $\mathbf{v} \in \mathbb{R}^n, \mathcal{X} \in G$. Following [20], we overload the left- and right- \oplus operations,

$$\begin{aligned} \text{left-}\oplus : G \times \mathbb{R}^n &\rightarrow G, \quad \mathcal{X} \oplus \mathbf{u} = \mathcal{X} \text{Exp}(\mathbf{u}), \\ \text{right-}\oplus : \mathbb{R}^n \times G &\rightarrow G, \quad \mathbf{u} \oplus \mathcal{X} = \text{Exp}(\mathbf{u})\mathcal{X}, \end{aligned} \quad (4)$$

and approximate the exponential map for $\|\mathbf{u}\| \approx 0$ using the right-Jacobian $\mathcal{J}_{r,G}(\cdot)$:

$$\text{Exp}_G(\mathbf{a} + \mathbf{u}) \approx \text{Exp}_G(\mathbf{a}) \oplus \mathcal{J}_{r,G}(\mathbf{a})\mathbf{u}. \quad (5)$$

The Lie algebra is important because it accommodates the error-state vectors of the respective filters [3]. In this work, we adopt a right-invariant error parameterization, defining the error-states as zero-mean Gaussian random variables as follows:

$$\begin{aligned} \boldsymbol{\xi}_i &:= \text{Log}_{\text{SE}_2(3) \times \mathbb{R}^6}(\mathcal{X}_i \bar{\mathcal{X}}_i^{-1}), \quad \boldsymbol{\xi}_i \sim \mathcal{N}(\mathbf{0}_{15,1}, \mathbf{P}_i), \\ \delta \mathbf{x}_i &:= \text{Log}_{\text{SO}(3) \times \mathbb{R}^{12}}(\mathbf{x}_i \bar{\mathbf{x}}_i^{-1}), \quad \delta \mathbf{x}_i \sim \mathcal{N}(\mathbf{0}_{15,1}, \boldsymbol{\Sigma}_i). \end{aligned} \quad (6)$$

The exponential, logarithmic, and right-Jacobians for the isolated Lie groups $SE_2(3)$ and $SO(3)$ are detailed in [17, Appendix I]. Their algebraic extension to the Cartesian product with \mathbb{R}^k vector spaces is straightforwardly obtained by forming block-diagonal matrices composed of the original group operators and identity matrices of matching dimensions.

4 Motivating Example

We start by motivating the proposed formulation, IterIEKF, with a simple example containing three landmarks and almost noise-free measurements (see Fig. 1). This example can be considered the extended 3D version of the motivating example presented in [17, Section IV]. Let \mathcal{X} be the current true state of the MAV; we assume at this moment that the robot can measure, with almost noise-free conditions, its relative position to three landmarks, \mathbf{b}_1 , \mathbf{b}_2 , and \mathbf{b}_3 . Each measurement defines a submanifold where the robot could have been located when obtaining that measurement. We denote this submanifold as the observed set $S_{\mathcal{X}^{-1}\mathbf{d}_k=\mathbf{y}_k}$ [17, Definition 1]. The three submanifolds originated by the three measurements are shown in Fig. 1a. At this moment, our noisy nominal state $\tilde{\mathcal{X}}$, with covariance \mathbf{P} , is far from the true state and receives all three measurements. We perform the update step with these measurements in a consecutive manner, using $SO(3)$ -EKF, IEKF, Iter $SO(3)$ -EKF, and IterIEKF. The results are shown in Figs. 1b, 1c, 1d, and 1e. We can observe that $SO(3)$ -EKF does not reach any observed set, while IEKF and Iter $SO(3)$ -EKF reach only the first. Finally, IterIEKF reaches the intersection of the three observed sets, which corresponds to the true state. This behavior is due to the main property of IterIEKF, which ensures that, after each update step, the estimated state is kept on the observed state manifold while the uncertainty is confined to its tangent space; i.e., there is no uncertainty transversal to the submanifold [12, Theorem 1]. This implies that, if the method converges, the final state after the last update step will lie exactly on the intersection of the three submanifolds [12, Theorem 2].

5 Discrete-Time Inertial Model

We assume the system dynamics is governed by IMU measurements, an old approach known as strapdown navigation [10]. In this approach, the high-frequency dynamics evolution is obtained by integrating the IMU measurements, i.e., the angular velocity $\tilde{\boldsymbol{\omega}}_{\mathcal{I},i}$ and linear acceleration $\tilde{\mathbf{a}}_{\mathcal{I},i}$. We denote by the subscript \mathcal{I} all quantities expressed in the IMU frame. We assume the measurements are piecewise constant over the time interval $[t_i, t_i + \Delta t]$ and that they are corrupted by additive white Gaussian noise and biases modeled as zero-mean random walks:

$$\tilde{\boldsymbol{\omega}}_{\mathcal{I},i} = \boldsymbol{\omega}_{\mathcal{I},i} + \mathbf{w}_{g,i} + \mathbf{b}_{g,i}, \quad \mathbf{w}_{g,i} \sim \mathcal{N}(\mathbf{0}_{3,1}, \mathbf{Q}_g), \quad (7)$$

$$\tilde{\mathbf{a}}_{\mathcal{I},i} = \mathbf{a}_{\mathcal{I},i} + \mathbf{w}_{a,i} + \mathbf{b}_{a,i}, \quad \mathbf{w}_{a,i} \sim \mathcal{N}(\mathbf{0}_{3,1}, \mathbf{Q}_a), \quad (8)$$

$$\mathbf{b}_{g,i+1} = \mathbf{b}_{g,i} + \mathbf{w}_{bg,i}\Delta t, \quad \mathbf{w}_{bg,i} \sim \mathcal{N}(\mathbf{0}_{3,1}, \mathbf{Q}_{bg}), \quad (9)$$

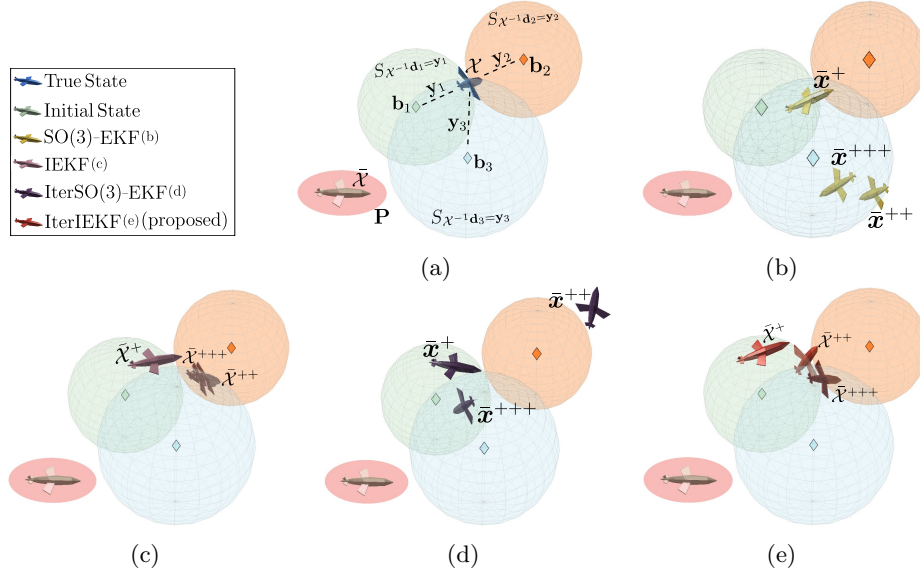


Fig. 1: a) Setup of a simple localization problem with three landmarks and almost noise-free measurements. b) Three consecutive updates with SO(3)-EKF. No update lies in the observed sets. c) Three consecutive updates with IEKF using almost noise-free measurements. Only the first update lies in the first observed set. d) Three consecutive updates with IterSO(3)-EKF. Only the first update lies in the observed sets. The other updates did not converge. e) Three consecutive updates with IterIEKF. All updates lie in the observed sets, with the last update lying on their intersection.

$$\mathbf{b}_{a,i+1} = \mathbf{b}_{a,i} + \mathbf{w}_{ba,i}\Delta t, \quad \mathbf{w}_{ba,i} \sim \mathcal{N}(\mathbf{0}_{3,1}, \mathbf{Q}_{ba}). \quad (10)$$

In this work, the nominal state is propagated through the system dynamics, while the error state is propagated through the linearized dynamics. The error state propagation is discussed in Section 7 for the invariant filters and Section 8 for the multiplicative filters. The system dynamics for all filters considered in this work are governed by the IMU inputs and given by [19, 18]:

$$\begin{aligned} \bar{\mathbf{x}}_{i|i-1} &:= \mathcal{F}_{i-1}(\bar{\mathbf{x}}_{i-1}, \tilde{\boldsymbol{\omega}}_{\mathcal{I},i-1}, \tilde{\mathbf{a}}_{\mathcal{I},i-1}, \Delta t) \\ &\approx \begin{bmatrix} \bar{\mathbf{R}}_{i-1} \oplus (\tilde{\boldsymbol{\omega}}_{\mathcal{I},i-1} - \bar{\mathbf{b}}_{g,i-1})\Delta t \\ \tilde{\mathbf{v}}_{i-1} + [\bar{\mathbf{R}}_{i-1}(\tilde{\mathbf{a}}_{\mathcal{I},i-1} - \bar{\mathbf{b}}_{a,i-1}) + \mathbf{g}]\Delta t \\ \bar{\mathbf{p}}_{i-1} + \tilde{\mathbf{v}}_{i-1}\Delta t + [\bar{\mathbf{R}}_{i-1}(\tilde{\mathbf{a}}_{\mathcal{I},i-1} - \bar{\mathbf{b}}_{a,i-1}) + \mathbf{g}]\frac{\Delta t^2}{2} \\ \bar{\mathbf{b}}_{g,i-1} \\ \bar{\mathbf{b}}_{a,i-1} \end{bmatrix}, \end{aligned} \quad (11)$$

where $\mathbf{g} := [0, 0, -9.81]^T$ and the nominal biases are kept constant during the propagation step. Notice that Eq. 11 is also used to obtain $\bar{\mathcal{X}}_{i|i-1}$ [5].

6 3D Landmark Measurement Model

Let \mathbf{b}_k represent a known landmark in the scene where the MAV is navigating. The MAV can measure the relative position of the landmark \mathbf{b}_k at instant t_i with respect to its IMU frame \mathcal{I} , which is denoted as $\mathbf{y}_{k,i}$. This measurement model can be expressed as follows:

$$\mathbf{y}_{k,i} = \mathbf{R}_i^T (\mathbf{b}_k - \mathbf{p}_i) + \mathbf{n}_{k,i}, \quad \mathbf{n}_{k,i} \sim \mathcal{N}(\mathbf{0}_{3,1}, \mathbf{N}_{k,i}), \quad (12)$$

or alternatively through the group action of $\text{SE}_2(3) \times \mathbb{R}^6$ required by invariant filter formulations [3]:

$$\begin{aligned} \tilde{\mathbf{y}}_{k,i} &:= \begin{pmatrix} \mathbf{R}_i^T (\mathbf{b}_k - \mathbf{p}_i) + \mathbf{n}_{k,i} \\ 0 \\ 1 \\ \mathbf{0}_{7,1} \end{pmatrix} \\ &= \begin{bmatrix} \begin{bmatrix} \mathbf{R}_i^T & -\mathbf{R}_i^T \mathbf{v}_i & -\mathbf{R}_i^T \mathbf{p}_i \\ \mathbf{0}_{1,3} & 1 & 0 \\ \mathbf{0}_{1,3} & 0 & 1 \end{bmatrix} & \mathbf{0}_{5,7} \\ & \begin{bmatrix} \mathbf{I}_6 & \begin{bmatrix} -\mathbf{b}_{g,i} \\ -\mathbf{b}_{a,i} \end{bmatrix} \\ \mathbf{0}_{1,6} & 1 \end{bmatrix} \end{bmatrix} \begin{pmatrix} \mathbf{b}_k \\ 0 \\ 1 \\ \mathbf{0}_{7,1} \end{pmatrix} + \begin{pmatrix} \mathbf{n}_{k,i} \\ \mathbf{0}_{9,1} \end{pmatrix} \\ &:= \mathcal{X}_i^{-1} \mathbf{d}_k + \tilde{\mathbf{n}}_{k,i}, \end{aligned} \quad (13)$$

where $\tilde{\mathbf{n}}_{k,i} \sim \mathcal{N}(\mathbf{0}_{12,1}, \tilde{\mathbf{N}}_{k,i} := \text{diag}(\mathbf{N}_{k,i}, \mathbf{0}_{9,9}))$.

When a set of landmarks $\{\mathbf{b}_k\}_{k=1}^K$ is observed simultaneously at the same time instant t_i , Eq. (12) can be stacked into a single consolidated measurement vector $\mathbf{y}_i \in \mathbb{R}^{3K}$ given by:

$$\mathbf{y}_i := \begin{pmatrix} \mathbf{y}_{1,i} \\ \vdots \\ \mathbf{y}_{K,i} \end{pmatrix} = \begin{pmatrix} \mathbf{R}_i^T (\mathbf{b}_1 - \mathbf{p}_i) \\ \vdots \\ \mathbf{R}_i^T (\mathbf{b}_K - \mathbf{p}_i) \end{pmatrix} + \bar{\mathbf{n}}_i, \quad (14)$$

where $\bar{\mathbf{n}}_i \sim \mathcal{N}(\mathbf{0}_{3K,1}, \bar{\mathbf{N}}_i := \text{diag}(\mathbf{N}_{1,i}, \dots, \mathbf{N}_{K,i}))$, while Eq. (13) is stacked to form the augmented measurement vector $\tilde{\mathbf{y}}_i \in \mathbb{R}^{12K}$:

$$\begin{aligned} \tilde{\mathbf{y}}_i &:= \begin{pmatrix} \tilde{\mathbf{y}}_{1,i} \\ \vdots \\ \tilde{\mathbf{y}}_{K,i} \end{pmatrix} = \begin{bmatrix} \mathcal{X}_i^{-1} & \mathbf{0}_{12,12} & \cdots & \mathbf{0}_{12,12} \\ \mathbf{0}_{12,12} & \mathcal{X}_i^{-1} & \cdots & \mathbf{0}_{12,12} \\ \vdots & \vdots & \ddots & \vdots \\ \mathbf{0}_{12,12} & \mathbf{0}_{12,12} & \cdots & \mathcal{X}_i^{-1} \end{bmatrix} \begin{pmatrix} \mathbf{d}_1 \\ \vdots \\ \mathbf{d}_K \end{pmatrix} + \begin{pmatrix} \tilde{\mathbf{n}}_{1,i} \\ \vdots \\ \tilde{\mathbf{n}}_{K,i} \end{pmatrix} \\ &:= \mathcal{X}_{\text{aug},i}^{-1} \mathbf{d} + \mathbf{n}_{\text{aug},i}. \end{aligned} \quad (15)$$

In practical applications, the measurement model in Eq. (12) is typically composed with an observation function determined by the sensing modality used to

detect the landmarks. For monocular and stereo cameras, this observation function is given by the perspective projection of the landmark onto the image plane, whereas LiDAR and RGB-D sensors provide direct three-dimensional measurements (or equivalently range-based measurements) of the landmark. Although such sensor-specific observation models are omitted here for simplicity, they can be readily incorporated into the proposed estimation framework by composing Eq. (12) with the corresponding observation function [8].

7 IEKF and IterIEKF

In this section, we describe the prediction and update steps for both the IEKF and IterIEKF formulations.

7.1 Prediction Step for Invariant Filtering

The prediction step for both IEKF and IterIEKF is identical and corresponds to the propagation of the right-invariant error $\boldsymbol{\xi}_i$. This is obtained by linearizing the error kinematics:

$$\boldsymbol{\xi}_{i|i-1} = \text{Log}_{\text{SE}_2(3) \times \mathbb{R}^6}(\mathcal{X}_i \bar{\mathcal{X}}_{i|i-1}^{-1}) \approx \mathbf{A}_{i-1} \boldsymbol{\xi}_{i-1} + \mathbf{B}_{i-1} \mathbf{w}_{i-1}, \quad (16)$$

where $\mathbf{w}_{i-1} \sim \mathcal{N}(\mathbf{0}_{12,1}, \mathbf{Q}_{i-1})$, with the grouped noise covariance defined as $\mathbf{Q}_{i-1} := \text{diag}(\mathbf{Q}_{g,i-1}, \mathbf{Q}_{a,i-1}, \mathbf{Q}_{bg,i-1}, \mathbf{Q}_{ba,i-1})$, and the system matrices defined as [5, 18]:

$$\mathbf{G}_{i-1} = -\bar{\mathbf{R}}_{i|i-1} \mathcal{J}_r \left((\tilde{\omega}_{\mathcal{I},i-1} - \bar{\mathbf{b}}_{g,i-1}) \Delta t \right) \Delta t, \quad (17)$$

$$\mathbf{A}_{i-1} = \begin{bmatrix} \mathbf{I}_3 & \mathbf{0}_3 & \mathbf{0}_3 & \mathbf{G}_{i-1} & \mathbf{0}_3 \\ \mathbf{g}^\wedge \Delta t & \mathbf{I}_3 & \mathbf{0}_3 & \bar{\mathbf{v}}_{i|i-1}^\wedge \mathbf{G}_{i-1} & -\bar{\mathbf{R}}_{i-1} \Delta t \\ \mathbf{g}^\wedge \Delta t^2 / 2 & \mathbf{I}_3 \Delta t & \mathbf{I}_3 & \bar{\mathbf{p}}_{i|i-1}^\wedge \mathbf{G}_{i-1} & -\bar{\mathbf{R}}_{i-1} \Delta t^2 / 2 \\ \mathbf{0}_3 & \mathbf{0}_3 & \mathbf{0}_3 & \mathbf{I}_3 & \mathbf{0}_3 \\ \mathbf{0}_3 & \mathbf{0}_3 & \mathbf{0}_3 & \mathbf{0}_3 & \mathbf{I}_3 \end{bmatrix}, \quad (18)$$

$$\mathbf{B}_{i-1} = \begin{bmatrix} \mathbf{G}_{i-1} & \mathbf{0}_3 & \mathbf{0}_3 & \mathbf{0}_3 \\ \bar{\mathbf{v}}_{i|i-1}^\wedge \mathbf{G}_{i-1} & -\bar{\mathbf{R}}_{i-1} \Delta t & \mathbf{0}_3 & \mathbf{0}_3 \\ \bar{\mathbf{p}}_{i|i-1}^\wedge \mathbf{G}_{i-1} & -\bar{\mathbf{R}}_{i-1} \Delta t^2 / 2 & \mathbf{0}_3 & \mathbf{0}_3 \\ \mathbf{0}_3 & \mathbf{0}_3 & \mathbf{I}_3 \Delta t & \mathbf{0}_3 \\ \mathbf{0}_3 & \mathbf{0}_3 & \mathbf{0}_3 & \mathbf{I}_3 \Delta t \end{bmatrix}. \quad (19)$$

From this linearization, the state covariance is propagated via:

$$\mathbf{P}_{i|i-1} \approx \mathbf{A}_{i-1} \mathbf{P}_{i-1} \mathbf{A}_{i-1}^T + \mathbf{B}_{i-1} \mathbf{Q}_{i-1} \mathbf{B}_{i-1}^T. \quad (20)$$

7.2 Update Step for Invariant Filtering

We define the innovation for the invariant filtering update step using the algebraic structures from Eq. (13). For a right-invariant error definition, the innovation vector is expressed as [3]:

$$\begin{aligned}
\mathbf{z}_{k,i} &:= \bar{\mathcal{X}}_{i|i-1} \tilde{\mathbf{y}}_{k,i} - \mathbf{d}_k \\
&= \bar{\mathcal{X}}_{i|i-1} \mathcal{X}_i^{-1} \mathbf{d}_k - \mathbf{d}_k + \bar{\mathcal{X}}_{i|i-1} \tilde{\mathbf{n}}_{k,i} \\
&= \delta \mathcal{X}_i^{-1} \mathbf{d}_k - \mathbf{d}_k + \bar{\mathcal{X}}_{i|i-1} \tilde{\mathbf{n}}_{k,i} \\
&= \text{Exp}(\boldsymbol{\xi}_i)^{-1} \mathbf{d}_k - \mathbf{d}_k + \bar{\mathcal{X}}_{i|i-1} \tilde{\mathbf{n}}_{k,i},
\end{aligned} \tag{21}$$

where $\delta \mathcal{X}_i := \mathcal{X}_i \bar{\mathcal{X}}_{i|i-1}^{-1} := \text{Exp}(\boldsymbol{\xi}_i)$ represents the right-invariant state error. The standard first-order Lie group approximation $\text{Exp}(\boldsymbol{\xi}_i)^{-1} \approx \mathbf{I} - \boldsymbol{\xi}_i^\wedge$ is applied to simplify the deterministic component:

$$\begin{aligned}
\text{Exp}(\boldsymbol{\xi}_i)^{-1} \mathbf{d}_k - \mathbf{d}_k &\approx -\boldsymbol{\xi}_i^\wedge \mathbf{d}_k \\
&= - \begin{bmatrix} \boldsymbol{\xi}_{i, \text{SE}_2(3)}^\wedge & \mathbf{0}_{5,7} \\ \mathbf{0}_{7,5} & \boldsymbol{\xi}_{i, \mathbb{R}^6}^\wedge \end{bmatrix} \mathbf{d}_k \\
&= - \begin{bmatrix} (\boldsymbol{\xi}_i^{\mathbf{R}})^\wedge \mathbf{b}_k + \boldsymbol{\xi}_i^{\mathbf{y}}(0) + \boldsymbol{\xi}_i^{\mathbf{p}}(1) + \boldsymbol{\xi}_i^{\mathbf{b}^g}(0) \\ \mathbf{0}_{1,3}(\mathbf{b}_k) + 0(0) + 0(1) \\ \mathbf{0}_{1,3}(\mathbf{b}_k) + 0(0) + 0(1) \\ \mathbf{0}_{1,3}(\boldsymbol{\xi}_i^{\mathbf{b}^g}) \\ \mathbf{0}_{1,3}(\boldsymbol{\xi}_i^{\mathbf{b}^a}) \end{bmatrix} \\
&= \begin{bmatrix} \mathbf{b}_k^\wedge & \mathbf{0}_3 & -\mathbf{I}_3 & \mathbf{0}_{3,6} \\ \mathbf{0}_{9,3} & \mathbf{0}_{9,3} & \mathbf{0}_{9,3} & \mathbf{0}_{9,6} \end{bmatrix} \begin{bmatrix} \boldsymbol{\xi}_i^{\mathbf{R}} \\ \boldsymbol{\xi}_i^{\mathbf{y}} \\ \boldsymbol{\xi}_i^{\mathbf{p}} \\ \boldsymbol{\xi}_i^{\mathbf{b}^g} \\ \boldsymbol{\xi}_i^{\mathbf{b}^a} \end{bmatrix} := \mathbf{H}_k \boldsymbol{\xi}_i.
\end{aligned} \tag{22}$$

Substituting this back into Eq. (21) yields the linearized innovation:

$$\mathbf{z}_{k,i} \approx \mathbf{H}_k \boldsymbol{\xi}_i + \hat{\mathbf{n}}_{k,i}, \tag{23}$$

where $\hat{\mathbf{n}}_{k,i} \sim \mathcal{N}(\mathbf{0}_{12,1}, \hat{\mathbf{N}}_{k,i} := \bar{\mathcal{X}}_{i|i-1} \hat{\mathbf{N}}_{k,i} \bar{\mathcal{X}}_{i|i-1}^T)$.

Given that the trailing rows of $\mathbf{z}_{k,i}$ are zero, the formulation can be reduced down to a 3-dimensional subsystem by projecting out the top block:

$$\tilde{\mathbf{z}}_{k,i} := [\mathbf{z}_{k,i}]_{1:3} \approx \tilde{\mathbf{H}}_{k,i} \boldsymbol{\xi}_i + \hat{\mathbf{n}}_{k,i}, \tag{24}$$

where the reduced measurement matrix is:

$$\tilde{\mathbf{H}}_{k,i} := [\mathbf{b}_k^\wedge \ \mathbf{0}_3 \ -\mathbf{I}_3 \ \mathbf{0}_{3,6}], \tag{25}$$

and $\hat{\mathbf{n}}_{k,i} \sim \mathcal{N}(\mathbf{0}_{3,1}, \hat{\mathbf{N}}_{k,i} := \bar{\mathbf{R}}_{i|i-1} \mathbf{N}_{k,i} \bar{\mathbf{R}}_{i|i-1}^T)$.

For a simultaneous collection of K visual or spatial landmarks, the measurement structures are vertically stacked into a unified system framework:

$$\mathbf{z}_i = \begin{pmatrix} \tilde{\mathbf{z}}_{1,i} \\ \vdots \\ \tilde{\mathbf{z}}_{K,i} \end{pmatrix} = \begin{bmatrix} \mathbf{b}_1^\wedge & \mathbf{0}_3 & -\mathbf{I}_3 & \mathbf{0}_{3,6} \\ \vdots & \vdots & \vdots & \vdots \\ \mathbf{b}_K^\wedge & \mathbf{0}_3 & -\mathbf{I}_3 & \mathbf{0}_{3,6} \end{bmatrix} \boldsymbol{\xi}_i + \begin{pmatrix} \hat{\mathbf{n}}_{1,i} \\ \vdots \\ \hat{\mathbf{n}}_{K,i} \end{pmatrix} = \mathbf{H}_i \boldsymbol{\xi}_i + \tilde{\mathbf{n}}_i, \quad (26)$$

where the collective stacked noise distribution tracks as

$$\tilde{\mathbf{n}}_i \sim \mathcal{N}(\mathbf{0}_{3K,1}, \tilde{\mathbf{N}}_i := \text{diag}(\hat{\mathbf{N}}_{1,i}, \dots, \hat{\mathbf{N}}_{K,i})). \quad (27)$$

The main difference between IterIEKF and IEKF is that instead of performing the linearization in Eq. 23 once per update, it applies a Gauss-Newton iterative method to linearize the innovation multiple times until convergence [12]. For the right-invariant error, this Gauss-Newton Sequence was obtained in [17]. We adapted this loop to be able to handle K visible landmarks, resulting in the following:

$$\Phi^j = \text{Exp}_{\text{SO}(3)}(-[\boldsymbol{\xi}_i^j]_{1:3}), \quad (28)$$

$$\mathbf{f}_k^j = [\text{Exp}(-\boldsymbol{\xi}_i^j) \mathbf{d}_k - \mathbf{d}_k]_{1:3}, \quad k = 1, \dots, K, \quad (29)$$

$$\mathbf{H}_i^j = \text{diag}(\underbrace{\Phi^j, \dots, \Phi^j}_{K \text{ times}}) \mathbf{H}_i \mathcal{J}_{r, \text{SE}_2(3) \times \mathbb{R}^6}(-\boldsymbol{\xi}_i^j), \quad (30)$$

$$\mathbf{S}_i^j = \mathbf{H}_i^j \mathbf{P}_{i|i-1} (\mathbf{H}_i^j)^T + \tilde{\mathbf{N}}_i, \quad (31)$$

$$\mathbf{K}_i^j = \mathbf{P}_{i|i-1} (\mathbf{H}_i^j)^T (\mathbf{S}_i^j)^{-1}, \quad (32)$$

$$\boldsymbol{\xi}_i^{j+1} = \mathbf{K}_i^j (\mathbf{z}_i - \text{vec}(\mathbf{f}_1^j, \dots, \mathbf{f}_K^j) + \mathbf{H}_i^j \boldsymbol{\xi}_i^j), \quad (33)$$

$$\boldsymbol{\xi}_i^0 := \mathbf{0}_{15,1}. \quad (34)$$

Finally, let l denote the last iteration, then the update step for the right-invariant error IterIEKF is given as follows:

$$\hat{\boldsymbol{\xi}}_i := \boldsymbol{\xi}_i^l, \quad (35)$$

$$\bar{\mathcal{X}}_i := \bar{\mathcal{X}}_{i|i} := \hat{\boldsymbol{\xi}}_i \oplus \bar{\mathcal{X}}_{i|i-1}, \quad (36)$$

$$\mathbf{P}_i := \mathbf{P}_{i|i} = (\mathbf{I}_{15} - \mathbf{K}_i^0 \mathbf{H}_i^0) \mathbf{P}_{i|i-1}, \quad (37)$$

To obtain the last iteration, we implemented as a stopping criterion the condition $\|\boldsymbol{\xi}^{j-1} - \boldsymbol{\xi}^j\| < \delta$, where $\delta = 10^{-4}$. We also implemented a second optional stopping criterion based on the computation of the loss in [17, Eq. 34]. If it increases, the algorithm stops.

8 SO(3)-EKF and IterSO(3)-EKF

In this section, we describe the prediction and update steps for both the standard SO(3)-EKF and the IterSO(3)-EKF, also widely known as Multiplicative-EKF [16]. These formulations serve as the non-invariant reference baselines for our comparative study.

8.1 Prediction Step for Multiplicative Filtering

The prediction step for these filters corresponds to the propagation of the standard multiplicative local error state $\delta \mathbf{x}_i$. This is obtained by linearizing the discrete-time error kinematics around the nominal state trajectory [19]:

$$\delta \mathbf{x}_{i|i-1} = \text{Log}_{\text{SO}(3) \times \mathbb{R}^{12}}(\mathbf{x}_i \bar{\mathbf{x}}_{i|i-1}^{-1}) \approx \bar{\mathbf{A}}_{i-1} \delta \mathbf{x}_{i-1} + \bar{\mathbf{B}}_{i-1} \mathbf{w}_{i-1}, \quad (38)$$

where:

$$\mathbf{F}_{i-1} = -[\bar{\mathbf{R}}_{i-1}(\tilde{\mathbf{a}}_{\mathcal{I},i-1} - \bar{\mathbf{b}}_{a,i-1})]^\wedge, \quad (39)$$

$$\bar{\mathbf{A}}_{i-1} = \begin{bmatrix} \mathbf{I}_3 & \mathbf{0}_3 & \mathbf{0}_3 & \mathbf{G}_{i-1} & \mathbf{0}_3 \\ \mathbf{F}_{i-1} \Delta t & \mathbf{I}_3 & \mathbf{0}_3 & \mathbf{0}_3 & -\bar{\mathbf{R}}_{i-1} \Delta t \\ \mathbf{F}_{i-1} \frac{\Delta t^2}{2} & \mathbf{I}_3 \Delta t & \mathbf{I}_3 & \mathbf{0}_3 & -\bar{\mathbf{R}}_{i-1} \frac{\Delta t^2}{2} \\ \mathbf{0}_3 & \mathbf{0}_3 & \mathbf{0}_3 & \mathbf{I}_3 & \mathbf{0}_3 \\ \mathbf{0}_3 & \mathbf{0}_3 & \mathbf{0}_3 & \mathbf{0}_3 & \mathbf{I}_3 \end{bmatrix}, \quad (40)$$

$$\bar{\mathbf{B}}_{i-1} = \begin{bmatrix} \mathbf{G}_{i-1} & \mathbf{0}_3 & \mathbf{0}_3 & \mathbf{0}_3 \\ \mathbf{0}_3 & -\bar{\mathbf{R}}_{i-1} \Delta t & \mathbf{0}_3 & \mathbf{0}_3 \\ \mathbf{0}_3 & -\bar{\mathbf{R}}_{i-1} \frac{\Delta t^2}{2} & \mathbf{0}_3 & \mathbf{0}_3 \\ \mathbf{0}_3 & \mathbf{0}_3 & \mathbf{I}_3 \Delta t & \mathbf{0}_3 \\ \mathbf{0}_3 & \mathbf{0}_3 & \mathbf{0}_3 & \mathbf{I}_3 \Delta t \end{bmatrix}. \quad (41)$$

Using this linearization, the state error covariance Σ is propagated forward in time through:

$$\Sigma_{i|i-1} \approx \bar{\mathbf{A}}_{i-1} \Sigma_{i-1} \bar{\mathbf{A}}_{i-1}^T + \bar{\mathbf{B}}_{i-1} \mathbf{Q}_{i-1} \bar{\mathbf{B}}_{i-1}^T. \quad (42)$$

8.2 Update Step for Multiplicative Filtering

For the multiplicative baseline, the measurement innovation is derived directly from the standard observation vector mapping in Eq. (12). Expanding using standard multiplicative perturbation steps ($\mathbf{R}_i \approx (\delta \phi_i) \oplus \bar{\mathbf{R}}_i$ and $\mathbf{p}_i = \bar{\mathbf{p}}_i + \delta \mathbf{p}_i$), the measurement innovation yields:

$$\begin{aligned} \delta \mathbf{z}_{k,i} &:= \mathbf{y}_{k,i} - \bar{\mathbf{R}}_i^T(\mathbf{b}_k - \bar{\mathbf{p}}_i) \\ &= (\delta \phi_i \oplus \bar{\mathbf{R}}_i)^T(\mathbf{b}_k - \bar{\mathbf{p}}_i - \delta \mathbf{p}_i) - \bar{\mathbf{R}}_i^T(\mathbf{b}_k - \bar{\mathbf{p}}_i) + \mathbf{n}_{k,i} \\ &\approx \bar{\mathbf{R}}_i^T(-\delta \phi_i^\wedge)(\mathbf{b}_k - \bar{\mathbf{p}}_i) - \bar{\mathbf{R}}_i^T \delta \mathbf{p}_i + \mathbf{n}_{k,i} \\ &= \bar{\mathbf{R}}_i^T(\mathbf{b}_k - \bar{\mathbf{p}}_i)^\wedge \delta \phi_i - \bar{\mathbf{R}}_i^T \delta \mathbf{p}_i + \mathbf{n}_{k,i}, \end{aligned} \quad (43)$$

which yields the measurement Jacobian matrix:

$$\bar{\mathbf{H}}_{k,i}(\bar{\mathbf{x}}_i) := [\bar{\mathbf{R}}_i^T(\mathbf{b}_k - \bar{\mathbf{p}}_i)^\wedge \mathbf{0}_3 - \bar{\mathbf{R}}_i^T \mathbf{0}_{3,6}]. \quad (44)$$

For a tracking sequence containing K visible spatial features, the observation parameters are vertically concatenated:

$$\begin{aligned} \mathbf{f}_k(\bar{\mathbf{x}}_i) &= \bar{\mathbf{R}}_i^T(\mathbf{b}_k - \bar{\mathbf{p}}_i), \quad k = 1, \dots, K, \\ \delta \mathbf{z}_i = \mathbf{y}_i - \begin{bmatrix} \mathbf{f}_1(\bar{\mathbf{x}}_i) \\ \vdots \\ \mathbf{f}_K(\bar{\mathbf{x}}_i) \end{bmatrix} &\approx \bar{\mathbf{H}}_i(\bar{\mathbf{x}}_i) \delta \mathbf{x}_i + \bar{\mathbf{n}}_i, \end{aligned} \quad (45)$$

where the complete augmented measurement Jacobian block $\bar{\mathbf{H}}_i(\bar{\mathbf{x}}_i) \in \mathbb{R}^{3K \times 15}$ is structured as:

$$\bar{\mathbf{H}}_i(\bar{\mathbf{x}}_i) := \begin{bmatrix} \bar{\mathbf{R}}_i^T(\mathbf{b}_1 - \bar{\mathbf{p}}_i)^\wedge \mathbf{0}_3 - \bar{\mathbf{R}}_i^T \mathbf{0}_{3,6} & & & & \\ & \vdots & \vdots & \vdots & \vdots \\ & & & & \\ \bar{\mathbf{R}}_i^T(\mathbf{b}_K - \bar{\mathbf{p}}_i)^\wedge \mathbf{0}_3 - \bar{\mathbf{R}}_i^T \mathbf{0}_{3,6} & & & & \end{bmatrix}. \quad (46)$$

Importantly, as highlighted by contrasting Eq. (44) with the invariant formulation in Eq. (25), the multiplicative measurement matrix explicitly depends on the absolute state estimate trajectories $(\bar{\mathbf{R}}_i, \bar{\mathbf{p}}_i)$.

The update sequence for the IterSO(3)-EKF tracks a localized Gauss-Newton optimization iteration scheme. We adapt the single-measurement sequence from [17, Eq. 59] into a stacked multi-landmark framework evaluated at optimization index j :

$$\mathbf{\Gamma}_i^j = \left(\delta\phi_i^j \oplus \bar{\mathbf{R}}_{i|i-1} \right)^T, \quad (47)$$

$$\bar{\mathbf{H}}_i^j = \begin{bmatrix} \mathbf{\Gamma}_i^j(\mathbf{b}_1 - \bar{\mathbf{p}}_{i|i-1} - \delta\mathbf{p}_i^j)^\wedge \mathcal{J}_{r,\text{SO}(3)}(-\delta\phi_i^j) \mathbf{0}_3 - \mathbf{\Gamma}_i^j \mathbf{0}_{3,6} & & & \\ & \vdots & \vdots & \vdots \\ \mathbf{\Gamma}_i^j(\mathbf{b}_K - \bar{\mathbf{p}}_{i|i-1} - \delta\mathbf{p}_i^j)^\wedge \mathcal{J}_{r,\text{SO}(3)}(-\delta\phi_i^j) \mathbf{0}_3 - \mathbf{\Gamma}_i^j \mathbf{0}_{3,6} & & & \end{bmatrix}, \quad (48)$$

$$\bar{\mathbf{S}}_i^j = \bar{\mathbf{H}}_i^j \Sigma_{i|i-1} (\bar{\mathbf{H}}_i^j)^T + \bar{\mathbf{N}}_i, \quad (49)$$

$$\bar{\mathbf{K}}_i^j = \Sigma_{i|i-1} (\bar{\mathbf{H}}_i^j)^T (\bar{\mathbf{S}}_i^j)^{-1}, \quad (50)$$

$$\delta\mathbf{x}_i^{j+1} = \bar{\mathbf{K}}_i^j \left(\mathbf{y}_i - \begin{bmatrix} \mathbf{f}_1(\bar{\mathbf{x}}_i^j) \\ \vdots \\ \mathbf{f}_K(\bar{\mathbf{x}}_i^j) \end{bmatrix} + \bar{\mathbf{H}}_i^j \delta\mathbf{x}_i^j \right), \quad (51)$$

initialized at the start of the optimization sequence with $\delta\mathbf{x}_i^0 := \mathbf{0}_{15,1}$. Letting l denote the final iteration step satisfying convergence, the posteriors are computed as:

$$\bar{\mathbf{x}}_i := \bar{\mathbf{x}}_{i|i} = \delta\mathbf{x}_i^l \oplus \bar{\mathbf{x}}_{i|i-1}, \quad (52)$$

$$\Sigma_i := \Sigma_{i|i} = (\mathbf{I}_{15} - \bar{\mathbf{K}}_i^l \bar{\mathbf{H}}_i^l) \Sigma_{i|i-1}. \quad (53)$$

The execution loop for the IterSO(3)-EKF employs identical convergence stopping criteria thresholds as those configured for the IterIEKF.

9 Results

We evaluate the performance of the proposed IterIEKF using a structured Monte Carlo simulation framework. The ground-truth inertial measurements are generated by solving the inverse kinematic problem over a known reference trajectory. Specifically, we extract the true state trajectories from the V2_01_easy dataset³

³ https://github.com/rpng/open_vins/blob/master/ov_data/euroc_mav/V2_01_easy.csv

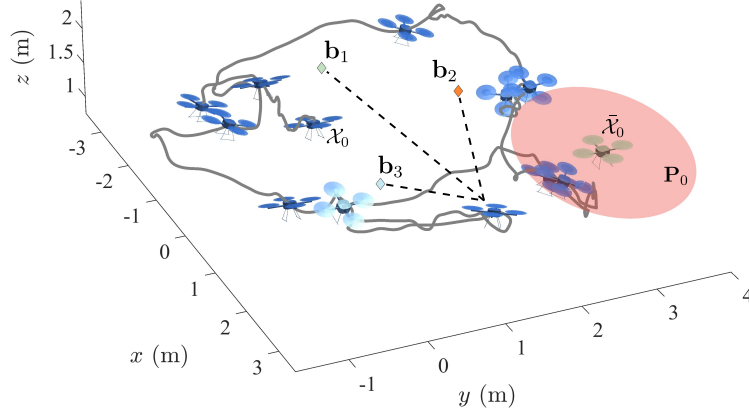


Fig. 2: V2_01_easy dataset trajectory (gray), MAV true state (blue), landmarks (diamonds), and a single MAV sample of the corrupted initial state configuration for the invariant estimators (green).

of the EuRoC MAV repository [7] and reconstruct ideal IMU inputs that satisfy the discrete-time system kinematics:

$$\begin{aligned}
 \mathcal{X}_{i+1} &= \mathcal{W}_i \Phi(\mathcal{X}_i) \mathcal{Y}_i(\boldsymbol{\omega}_{\mathcal{I},i}, \mathbf{a}_{\mathcal{I},i}) \\
 \Rightarrow (\mathcal{W}_i \Phi(\mathcal{X}_i))^{-1} \mathcal{X}_{i+1} &= \mathcal{Y}_i(\boldsymbol{\omega}_{\mathcal{I},i}, \mathbf{a}_{\mathcal{I},i}) \\
 \Rightarrow \left(\text{Exp}_{\text{SO}(3)}(\mathbf{a}), \mathbf{b} \right) &= \left(\text{Exp}_{\text{SO}(3)}(\boldsymbol{\omega}_{\mathcal{I},i} \Delta t), \mathbf{L} \mathbf{a}_{\mathcal{I},i} \right), \\
 \Rightarrow \boldsymbol{\omega}_{\mathcal{I},i} &= \frac{\mathbf{a}}{\Delta t}, \quad \mathbf{a}_{\mathcal{I},i} = \mathbf{L}^\dagger \mathbf{b}, \quad \mathcal{W}_i, \Phi, \mathcal{Y}_i \in \text{SE}_2(3),
 \end{aligned} \tag{54}$$

where the kinematic prediction model from Eq. (11) is reformulated as a composition of algebraic elements on $\text{SE}_2(3)$ [5]. The coupling matrix \mathbf{L} is defined as $\mathbf{L} = [\mathbf{I}_3 \Delta t; \mathbf{I}_3 \frac{\Delta t^2}{2}]$, and $\mathbf{L}^\dagger = (\mathbf{L}^T \mathbf{L})^{-1} \mathbf{L}^T$ represents its left pseudo-inverse. In addition to obtaining the true inertial measurements, we also artificially placed three landmarks in the world frame, $\mathbf{b}_1 = [-2.0, 1.0, 1.6]^T$, $\mathbf{b}_2 = [0.0, 2.0, 2.0]^T$ and $\mathbf{b}_3 = [1.0, 0.5, 1.5]^T$.

Across $N = 50$ localized Monte Carlo realizations, we corrupt the true initial state configuration, the proprioceptive inertial sequences, and the exteroceptive landmark updates with zero-mean white Gaussian noise structured as:

$$\begin{aligned}
 \mathbf{P}_0 &= \text{diag} \left(\left(\frac{\pi}{4} \right)^2 \mathbf{I}_3, 1.0^2 \mathbf{I}_3, 2.0^2 \mathbf{I}_3, 10^{-6} \mathbf{I}_3, 10^{-6} \mathbf{I}_3 \right), \\
 \mathbf{w}_{a,i} &\sim \mathcal{N}(\mathbf{0}_{3,1}, 1.6 \times 10^{-3} \mathbf{I}_3), \quad \mathbf{w}_{g,i} \sim \mathcal{N}(\mathbf{0}_{3,1}, 4.0 \times 10^{-6} \mathbf{I}_3), \\
 \mathbf{w}_{bg,i}, \mathbf{w}_{ba,i} &\sim \mathcal{N}(\mathbf{0}_{3,1}, 1.0 \times 10^{-6} \mathbf{I}_3), \quad \mathbf{n}_{k,i} \sim \mathcal{N}(\mathbf{0}_{3,1}, 1.0 \times 10^{-3} \mathbf{I}_3).
 \end{aligned} \tag{55}$$

During each initialization pass, the true baseline state is perturbed by an error displacement sample $\boldsymbol{\xi}_0 \sim \mathcal{N}(\mathbf{0}_{15,1}, \mathbf{P}_0)$. This generates the nominal starting

state for the invariant filters via $\bar{\mathbf{x}}_0 = (-\boldsymbol{\xi}_0) \oplus \mathcal{X}_0$, while the multiplicative variants initialize through $\bar{\mathbf{x}}_0 = (-\delta\mathbf{x}_0) \oplus \mathbf{x}_0$, with $\delta\mathbf{x}_0 = \mathbf{J}\boldsymbol{\xi}_0$ mapped via the state-space transformation Jacobian defined in [17, Eq. 76]. The trajectory trace and a sample visualization of this initialization are shown in Fig. 2. The simulated IMU feeds operate at 200 Hz, whereas landmark observations update at a reduced rate of 1 Hz with all landmarks visible during the entire trajectory, i.e., $K = 3$.

Filter statistical consistency is evaluated over all time horizons using the Average Normalized Estimation Error Squared (NEES) metric:

$$\begin{aligned} \text{NEES}_i^{\text{SE}_2(3) \times \mathbb{R}^6} &= \frac{1}{N} \sum_{n=1}^N (\boldsymbol{\xi}_i^n)^T (\mathbf{P}_i^n)^{-1} \boldsymbol{\xi}_i^n, \\ \text{NEES}_i^{\text{SO}(3) \times \mathbb{R}^{12}} &= \frac{1}{N} \sum_{n=1}^N (\delta\mathbf{x}_i^n)^T (\boldsymbol{\Sigma}_i^n)^{-1} \delta\mathbf{x}_i^n. \end{aligned} \quad (56)$$

Trajectory accuracy is quantified through the Mean Absolute Error (MAE) evaluated across the system’s observable state space, including the body-frame linear velocity ($\bar{\mathbf{R}}_{i|i}^T \bar{\mathbf{v}}_{i|i}$), global gravity vector orientation ($\bar{\mathbf{u}}_{i|i}$), and Euler attitude parameters (yaw $\bar{\psi}_{i|i}$, pitch $\bar{\phi}_{i|i}$, and roll $\bar{\theta}_{i|i}$). The error metric tracks as:

$$\text{MAE}_{\mathbf{x}} = \frac{1}{M} \sum_{i=1}^M e(\bar{\mathbf{x}}_{i|i}, \mathbf{x}_i), \quad (57)$$

where M defines the total number of timestamps across the mission duration. For position, velocity, and attitude states, $e(\cdot)$ corresponds to the standard Euclidean distance metric $e := \|\mathbf{x}_i - \bar{\mathbf{x}}_{i|i}\|$. For tracking the gravity vector direction, the metric is defined as the angular displacement $e := \arccos(\bar{\mathbf{u}}_{i|i} \cdot \mathbf{u}_i)$ to provide a physically intuitive representation of angular drift.

9.1 Accuracy and Consistency of the Observable State

The quantitative performance metrics across the $N = 50$ Monte Carlo simulation trials, consolidated in Table 1, reveal a performance disparity between the evaluated filtering paradigms under initial state corruption. The classical SO(3)-EKF exhibits the poorest performance, accumulating a substantial MAE of 9.363 m in position and 4.918 m/s in linear velocity due to the well-documented false observability problem, where state-dependent measurement Jacobians erroneously introduce spurious information along unobservable directions. While the IterSO(3)-EKF mitigates local linearization errors through iterative refinement loops, reducing the position and velocity MAE to 2.1 m and 1.331 m/s, respectively, it lacks geometric error parameterization and remains significantly less accurate than the standard single-step IEKF (0.511 m). In contrast, the proposed IterIEKF achieves state-of-the-art performance, outperforming the baseline IEKF by reducing position error to 0.096 m (an 81.12% reduction) and velocity error to 0.095 m/s (an 80.14% reduction). This remarkable tracking fidelity

highlights the benefit of fusing Lie-group error dynamics on $SE_2(3)$, which structurally decouple the error kinematics from the absolute trajectory to guarantee correct observability properties, with localized Gauss-Newton optimization loops that drive the estimated state precisely to the true intersection of the environmental landmark manifolds. The convergence of the estimated position, velocity and gravity direction are shown in Figs. 3a, 3b and 3c. The IterIEKF demonstrates superior convergence characteristics, rapidly aligning with the ground truth trajectory within the first 10s of operation, while the IEKF exhibits a slower convergence rate and larger steady-state error. The IterSO(3)-EKF, although improving upon the SO(3)-EKF, still fails to achieve comparable accuracy due to its inherent limitations in handling non-linearities and observability issues.

In Fig. 3d we show the NEES metric for the different filters, where the IterIEKF maintains a NEES value close to 15 (the error-state dimension), indicating good consistency, while the IEKF and IterSO(3)-EKF show higher NEES values, suggesting overconfidence in their estimates. The SO(3)-EKF exhibits the highest NEES values, confirming its poor consistency and reliability in state estimation under severe initial state corruption.

Table 1: Mean Absolute Error (MAE) and relative errors to IEKF (%) for different filtering methods. Smallest MAE is marked in bold.

Filters	MAE _{velocity} (m/s)	MAE _{gravity direction} (°)	MAE _{position} (m)
IEKF	0.48 (0%)	2.042 (0%)	0.511 (0%)
IterIEKF	0.095 (-80.135%)	0.661 (-67.641%)	0.096 (-81.117%)
SO(3)-EKF	4.918 (+925.35%)	11.244 (+450.7%)	9.363 (+1732.8%)
IterSO(3)-EKF	1.331 (+177.49%)	4.439 (+117.41%)	2.1 (+311.15%)

9.2 Attitude Estimation

The average attitude estimation (roll, pitch and yaw angles) computed in all Monte Carlo realizations is shown in Fig. 4. Overall, the proposed IterIEKF achieves the fastest convergence rate, settling almost 10 seconds ahead of the standard, single-step IEKF (see Fig. 4c). Interestingly, the IterIEKF exhibits a slightly prolonged settling time when converging the roll angle (Fig. 4a), whereas it experiences highly accelerated convergence characteristics in the pitch channel (Fig. 4b). Furthermore, both the classical SO(3)-EKF and its iterated counterpart, the IterSO(3)-EKF, demonstrate significantly slower response dynamics, though the IterSO(3)-EKF noticeably outperforms the baseline EKF due to its

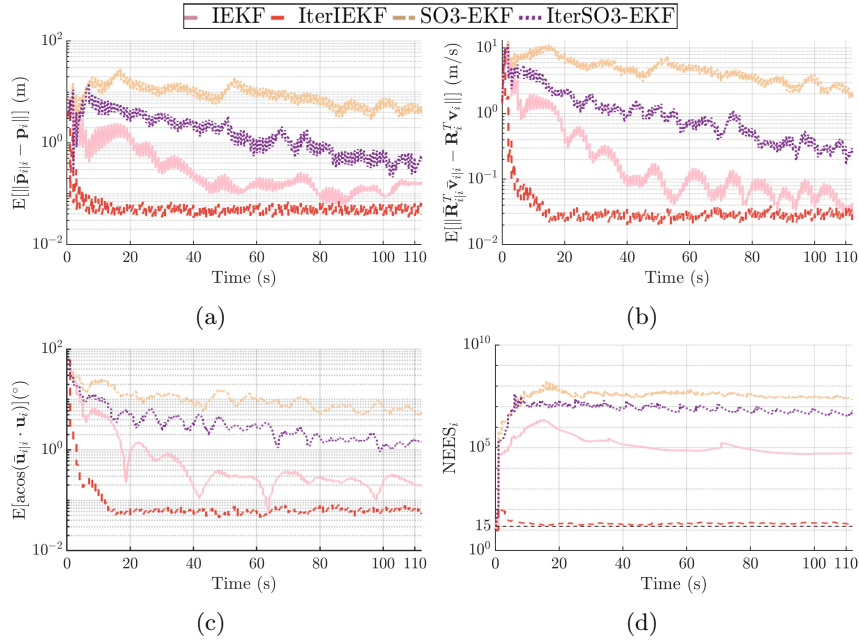


Fig. 3: Results of the numerical Monte Carlo experiment on the `V2.01_easy` dataset. a) Average error for the position. b) Average error for the velocity in the base frame. c) Average error for the gravity direction. d) Average NEES.

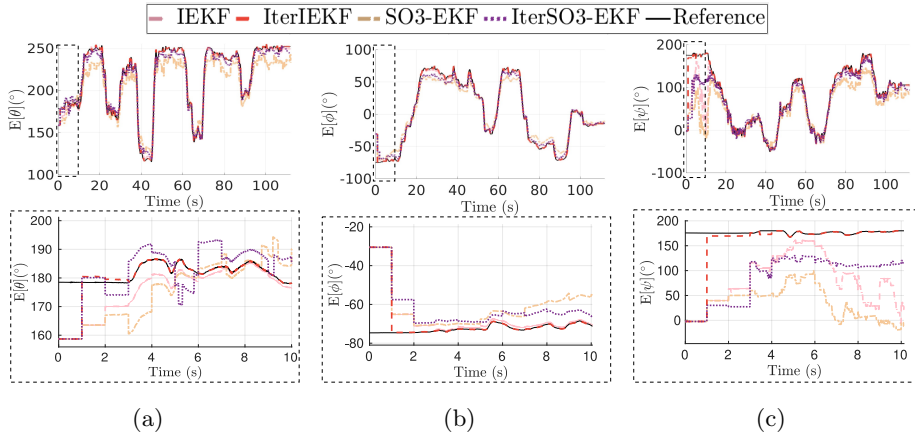


Fig. 4: Average attitude estimates obtained with different filters across all realizations. a) Estimate of the roll angle. b) Estimate of the pitch angle. c) Estimate of the yaw angle.

local optimization loops. These tracking profiles confirm that the IterIEKF pos-

sesses superior robustness against severe initial state corruption, providing the most reliable and highly consistent attitude estimation performance among all evaluated filters.

9.3 Bias Convergence Analysis

The relative estimation errors of the IMU bias for a representative single realization of the Monte Carlo simulation are illustrated in Fig. 5. Overall, a similar trend to the previous state trajectory evaluations is observed, with the proposed IterIEKF demonstrating superior convergence and lower residual errors compared to all baseline filters. Moreover, it can be observed in Figs. 5b and 5c that the invariant filters presented low steady-state error for the gyroscope biases. However, every evaluated filter, including the IterIEKF, experiences noticeable difficulty in accurately identifying the accelerometer biases, with the relative error persistently remaining above 1.0. This limitation underscores a core structural constraint of the current formulation: appending the sensor biases directly to the state space as a standard vector addition (\mathbb{R}^6) breaks the strict group-affine property of the system dynamics during the propagation step. Consequently, the propagation mechanics are not fully invariant with respect to the bias states. This observability and consistency mismatch could potentially be resolved by adopting the recently introduced Two-Frame Group (TFG) framework [3], a novel Lie group structure designed to embed accelerometer biases in a structurally invariant manner.

10 Conclusion

In this work, we have presented the first formulation and systematic evaluation of the Iterated Invariant Extended Kalman Filter tailored for 3D landmark-aided inertial navigation in MAVs. By parameterizing the system state error via right-invariant group actions on $SE_2(3)$, our framework structurally eliminates the false observability problem that plagues classical non-invariant architectures like the $SO(3)$ -EKF and Iter $SO(3)$ -EKF. Furthermore, by incorporating localized Gauss-Newton optimization loops directly into the invariant measurement update, the IterIEKF overcomes the linearization limitations of the standard single-step IEKF. Extensive Monte Carlo simulations based on a trajectory profile from the EuRoC MAV dataset demonstrate that the IterIEKF yields a profound performance leap, securing upwards of an 80% reduction in both position and linear velocity errors compared to the standard IEKF, while establishing superior NEES statistical consistency and highly accurate gravity vector alignment. While the IterIEKF demonstrates exceptional tracking robustness and prevents cross-state error corruption, online accelerometer biases remain poorly estimated. Future work aims to scale the proposed filter into a full SLAM framework that unifies invariant state estimation with online data association and unknown landmark map generation.

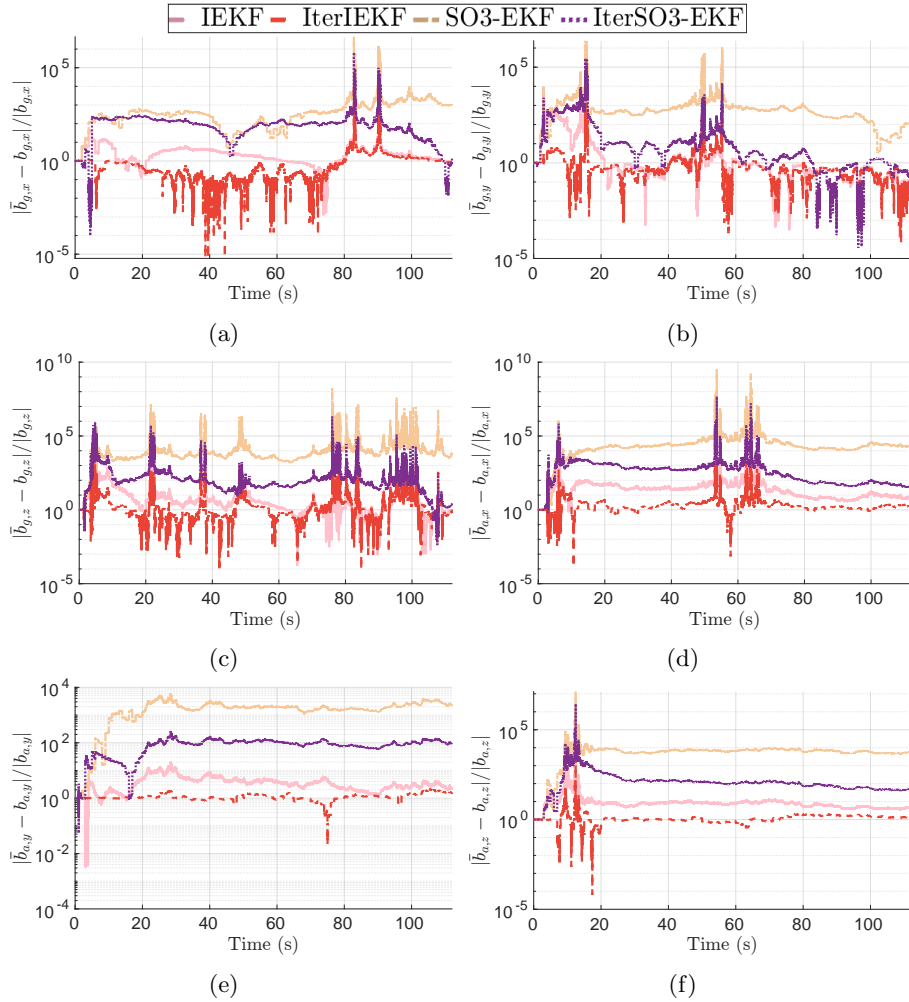


Fig. 5: Relative error for the estimates of the IMU bias obtained with different filters on one realization of the Monte Carlo simulation. a) Gyroscope bias in the x -axis. b) Gyroscope bias in the y -axis. c) Gyroscope bias in the z -axis. d) Accelerometer bias in the x -axis. e) Accelerometer bias in the y -axis. f) Accelerometer bias in the z -axis.

References

1. Barfoot, T.D.: State Estimation for Robotics. Cambridge Univ. Press (2024)
2. Barrau, A., Bonnabel, S.: The invariant extended Kalman filter as a stable observer. *IEEE Trans. Autom. Control* **62**(4), 1797–1812 (2016)
3. Barrau, A., Bonnabel, S.: The geometry of navigation problems. *IEEE Trans. Autom. Control* **68**(2), 689–704 (2022)

4. Bloesch, M., Burri, M., Omari, S., Hutter, M., Siegwart, R.: Iterated extended Kalman filter based visual-inertial odometry using direct photometric feedback. *Int. J. Robot. Res.* **36**(10), 1053–1072 (2017)
5. Brossard, M., Barrau, A., Chauchat, P., Bonnabel, S.: Associating uncertainty to extended poses for on Lie group IMU preintegration with rotating earth. *IEEE Trans. Robot.* **38**(2), 998–1015 (2021)
6. Brossard, M., Bonnabel, S., Barrau, A.: Invariant Kalman filtering for visual inertial SLAM. In: *Proc. Int. Conf. Inf. Fusion (FUSION)*. pp. 2021–2028 (2018)
7. Burri, M., Nikolic, J., Gohl, P., Schneider, T., Rehder, J., Omari, S., Achtelik, M.W., Siegwart, R.: The EuRoC micro aerial vehicle datasets. *Int. J. Robot. Res.* **35**(10), 1157–1163 (2016)
8. Debeunne, C., Vivet, D.: A review of visual-LiDAR fusion based simultaneous localization and mapping. *Sensors* **20**(7), 2068 (2020)
9. Dissanayake, M.W.M.G., Newman, P., Clark, S., Durrant-Whyte, H.F., Csorba, M.: A solution to the simultaneous localization and map building (SLAM) problem. *IEEE Trans. Robot. Autom.* **17**(3), 229–241 (2001)
10. Edwards Jr., A.: The state of strapdown inertial guidance and navigation. *Navigation* **18**(4), 386–401 (1971)
11. Elhousni, M., Huang, X.: A survey on visual map localization using LiDARs and cameras. *arXiv preprint arXiv:2208.03376* (2022)
12. Goffin, S., Barrau, A., Bonnabel, S., Brüls, O., Sacrè, P.: Iterated invariant extended Kalman filter (IterIEKF). *IEEE Trans. Autom. Control* **71**(5), 3380–3387 (2026)
13. He, D., Xu, W., Zhang, F.: Kalman filters on differentiable manifolds. *arXiv preprint arXiv:2102.03804* (2021)
14. Leonard, J.J., Durrant-Whyte, H.F., et al.: Mobile robot localization by tracking geometric beacons. *IEEE Trans. Robot. Autom.* **7**(3), 376–382 (1991)
15. Li, M., Mourikis, A.I.: High-precision, consistent EKF-based visual-inertial odometry. *Int. J. Robot. Res.* **32**(6), 690–711 (2013)
16. Markley, F.L.: Multiplicative vs. additive filtering for spacecraft attitude determination quaternion estimation. *J. Guid. Control Dyn.* **26**(2), 311–317 (2003)
17. Santana, H.M.S., Soares, J.C.V., Goffin, S., Nisticò, Y., Bonnabel, S., Semini, C., Meggiolaro, M.A.: Iterated invariant EKF for quadruped robot odometry. *arXiv preprint arXiv:2604.15449* (2026)
18. Santana, H.M.S., Soares, J.C.V., Nisticò, Y., Meggiolaro, M.A., Semini, C.: Proprioceptive state estimation for quadruped robots using invariant kalman filtering and scale-variant robust cost functions. In: *2024 IEEE-RAS 23rd International Conference on Humanoid Robots (Humanoids)*. pp. 213–220 (2024)
19. Solà, J.: Quaternion kinematics for the error-state Kalman filter. *arXiv preprint arXiv:1711.02508* (2017)
20. Solà, J., Deray, J., Atchuthan, D.: A micro Lie theory for state estimation in robotics. *arXiv preprint arXiv:1812.01537* (2018)
21. Trawny, N., Mourikis, A.I., Roumeliotis, S.I., Johnson, A.E., Montgomery, J.F.: Vision-aided inertial navigation for pin-point landing using observations of mapped landmarks. *J. Field Robot.* **24**(5), 357–378 (2007)